









LETTER | JULY 06 2023

Mid-infrared integrated silicon–germanium ring resonator with high Q-factor

Rémi Armand; Marko Perestjuk ; Alberto Della Torre ; Milan Sinobad; Arnan Mitchell ; Andreas Boes ; Jean-Michel Hartmann ; Jean-Marc Fedeli ; Vincent Reboud ; Pierre Brianceau; Alfredo De Rossi ; Sylvain Combrié ; Christelle Monat ; Christian Grillet 




APL Photonics 8, 071301 (2023)

<https://doi.org/10.1063/5.0149324>



CrossMark



THE ADVANCED MATERIALS MANUFACTURER®

yttrium iron garnet glassy carbon beamsplitters fused quartz additive manufacturing

zeolites III-IV semiconductors gallium lump copper nanoparticles organometallics

nano ribbons barium fluoride europium phosphors photonics infrared dyes

sapphire windows Nd:YAG epitaxial crystal growth ultra high purity materials transparent ceramics CIGS

spintronics raman substrates cerium oxide polishing powder cermet nanodispersions

silver nanoparticles perovskites surface functionalized nanoparticles MBE grade materials thin film

MOCVD beta-barium borate Os Ir Pt Au Ti Pd Ag Cu Zn Ga Ge As Se Br Kr

rare earth metals quantum dots Os Ir Pt Au Ti Pd Ag Cu Zn Ga Ge As Se Br Kr

osmium scintillation Ce:YAG Os Ir Pt Au Ti Pd Ag Cu Zn Ga Ge As Se Br Kr

refractory metals laser crystals Os Ir Pt Au Ti Pd Ag Cu Zn Ga Ge As Se Br Kr

antiferromagnetic materials niobate InAs wafers metamaterials borosilicate glass

25th Anniversary MOFs AuNPs YBCO superconductors InGaAs

ZnS CdTe indium tin oxide MgF2 rutile optical glass

perovskite crystals transparent ceramics diamond micropowder

Now Invent.™

www.americanelements.com

© 2001-2023, American Elements LLC, a U.S. Registered Trademark

The Next Generation of Material Science Catalogs

Mid-infrared integrated silicon-germanium ring resonator with high Q-factor

Cite as: APL Photon. 8, 071301 (2023); doi: 10.1063/5.0149324

Submitted: 5 March 2023 • Accepted: 19 June 2023 •

Published Online: 6 July 2023



Rémi Armand,¹ Marko Perestjuk,^{1,2,a)} Alberto Della Torre,¹ Milan Sinobad,³ Arnan Mitchell,² Andreas Boes,^{2,4,5} Jean-Michel Hartmann,⁶ Jean-Marc Fedeli,⁶ Vincent Reboud,⁶ Pierre Brianceau,⁶ Alfredo De Rossi,⁷ Sylvain Combré,⁷ Christelle Monat,¹ and Christian Grillet¹

AFFILIATIONS

¹ Université de Lyon, Institut des Nanotechnologies de Lyon (INL) UMR CNRS 5270, Ecole Centrale Lyon, 69131 Ecully, France

² School of Engineering, RMIT University, Melbourne, VIC 3001, Australia

³ Deutsches Elektronen-Synchrotron, 22607 Hamburg, Germany

⁴ Institute for Photonics and Advanced Sensing, The University of Adelaide, Adelaide, SA 5005, Australia

⁵ School of Electrical and Mechanical Engineering, The University of Adelaide, Adelaide, SA 5005, Australia

⁶ Université Grenoble Alpes, CEA-Leti, 38054 Grenoble, France

⁷ Thales Research and Technology, Campus Polytechnique, 91767 Palaiseau, France

^{a)} Author to whom correspondence should be addressed: marko.perestjuk@ec-lyon.fr

ABSTRACT

We report the realization of a silicon-germanium on silicon ring resonator with high Q-factor at mid-infrared wavelengths. The fabricated ring exhibits a loaded Q-factor of 236 000 at the operating wavelength of 4.18 μm . Considering the combined waveguide propagation losses and bending losses, which are measured to be below 0.2 dB/cm, even higher Q-factors could be achieved on this platform. Furthermore, our dispersion engineering of the waveguides should make these microrings suitable for nonlinear optical applications. These results pave the way for sensing applications and nonlinear optics in the mid-infrared range.

© 2023 Author(s). All article content, except where otherwise noted, is licensed under a Creative Commons Attribution (CC BY) license (<http://creativecommons.org/licenses/by/4.0/>). <https://doi.org/10.1063/5.0149324>

I. INTRODUCTION

The mid-infrared (MIR) wavelength range (between 3 and 15 μm) is attractive for sensing applications, as many molecules have strong fundamental absorption lines in this spectral region. Applications that benefit from this spectral range include environmental monitoring, defense and security, health care, and industrial process monitoring.¹ However, so far, the high cost and large size of MIR devices have slowed down the widespread use of this promising technology. Leveraging progress in group-IV photonic integrated circuits² and efforts made to integrate MIR components on chips with reduced cost, power consumption, and size should enable the large scale deployment of MIR technologies.

High quality factor ring (and racetrack) resonators are expected to play a crucial role in on-chip integrated sensing schemes. First, they could be used to generate optical frequency combs,³ and thus broadband MIR light sources for sensing devices, or they could serve

as the basis for dual comb spectroscopy.⁴ Second, rings can also be directly used to enhance the interaction between light and the analyte molecules surrounding the ring.⁵ Whether it be via detecting some changes in the resonance wavelength or linewidth, most of the sensing schemes exploiting microring resonators require a high quality factor (Q-factor) to improve the sensitivity and detection limit of the sensor.^{6,7}

High Q-factors in ring resonators have already been demonstrated in the SWIR range (Short Wavelength InfraRed range, below 3.5 μm) in the silicon on insulator (SOI)⁸ and the silicon nitride on insulator (SiNOI)⁹ platforms with intrinsic Q-factors reaching, respectively, 1.1×10^6 at 3.8 μm and 10^6 at 2.6 μm , and even in the MIR in silicon on sapphire (SOS)¹⁰ reaching a loaded Q of 151 000 at 4.4 μm . While the SOI, SiNOI, and SOS platforms are very interesting for SWIR and low MIR wavelengths, they suffer from high intrinsic losses due to absorption caused by the lower cladding material beyond ~ 3.5 and ~ 6.5 μm , respectively.¹ Approaches using

TABLE I. Experimentally demonstrated loaded Q-factors of integrated ring and racetrack resonators on Ge-based group IV photonics platforms in the MIR range.

References	Platform	Integrated	Wavelength (μm)	Perimeter (mm)	Q-factor
20	Ge-on-Si	Yes	3.8	0.44	1 700
21	Graded-index SiGe	Yes	7.7–8.6	1.97	3 200
22	Ge-on-Si	Yes	8.1–11.0	3.54	10 000
23	Ge-on-SOI	Yes	5.3	0.66	20 000
24	Ge	No	7.8	1.41	224 000
This work	SiGe-on-Si	Yes	4.18	1.57	236 000

suspended Si rings¹¹ and III–V photonics¹² have not yet managed to solve this issue either. Material platforms that have low optical losses across a broad range of the MIR spectrum are thus desired to leverage the full potential of this technology.

In this context, silicon–germanium (SiGe) and germanium (Ge) are promising materials, thanks to their CMOS compatibility and transparency window that extends up to 15 μm .^{1,13,14} Low-loss SiGe waveguides operating in the MIR range have been demonstrated,^{14,15} and their nonlinear properties were used for supercontinuum generation up to 8.5 μm in SiGe and 13 μm in graded-index SiGe.^{16–18} In pure Ge waveguides, supercontinuum generation was achieved up to 6 μm .¹⁹ So far, however, only a few SiGe and Ge ring resonator demonstrations have been reported in the MIR range, with moderate loaded Q-factors between 1700 and 20 000 (see Table I for details).^{20–23} Very recently, high-Q resonators on Ge have been reported with an intrinsic Q = 250 000 at 7.8 μm wavelength.²⁴ However, this was achieved using Ge disks on glass pillars, hence hindering the prospects for a full integration within a circuit, as desired for applications.

Here, we report the experimental demonstration of a high Q SiGe ring resonator with a loaded Q-factor of 236 000 at 4.18 μm wavelength. In addition, our measurements on serpentine waveguides show that bending losses become “negligible” beyond 250 μm radius, indicating that intrinsic Q-factors of microrings on this platform could be as high as 1 170 000. Such high Q resonators achieved in a platform that has a very large transparency window (potentially up to 15 μm) should allow us to leverage the full potential of the MIR technology for applications such as sensing and optical frequency comb generation.

II. RING RESONATOR DESIGN AND FABRICATION

Our platform consists of an air-cladded $\text{Si}_{0.6}\text{Ge}_{0.4}$ core waveguide on a Si substrate [Fig. 1(a)]. Our intended wavelength of operation is 4.18 μm . In addition, the relevance for sensing applications around this wavelength, for example for sensing carbon dioxide,²⁵ this spectral band was shown to be a sweet spot in terms of SiGe nonlinear properties.¹⁷ To determine the optical properties at

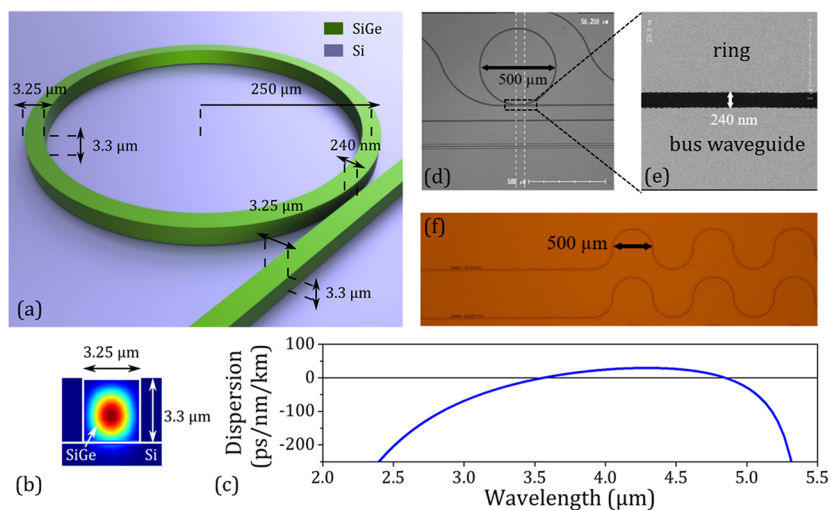


FIG. 1. (a) Ring resonator with dimensions, evanescently coupled to a bus waveguide on the SiGe platform. Air-cladded waveguides of $\text{Si}_{0.6}\text{Ge}_{0.4}$ ($n = 3.57$ at $\lambda = 4.18 \mu\text{m}$) on a Si substrate ($n = 3.42$) are used. (b) Mode profile of TE₀. (c) Dispersion parameter D as a function of wavelength λ for the chosen waveguide dimensions (single mode). A broad region of anomalous dispersion ($D > 0$) from $\lambda = 3.5$ – $4.8 \mu\text{m}$ is obtained. (d) SEM picture of the fabricated ring. (e) SEM picture of the gap between the ring and bus waveguide. (f) Optical microscope picture of the fabricated serpentine waveguides for determining bending losses.

this wavelength, especially the refractive indices, ellipsometry measurements were performed. The refractive index of the transparent SiGe layer at $4.18\ \mu\text{m}$ was $n = 3.57$ and, for the Si substrate, $n = 3.42$. Utilizing these values, we used the finite difference eigenmode (FDE) solver of Lumerical²⁶ to analyze the modal behavior and calculate the dispersion of the waveguides [including the material dispersion $n(\lambda)$]. An example for a mode profile (electric field intensity) of the fundamental mode in transverse-electric (TE) polarization is shown in Fig. 1(b).

As our long-term objective is the demonstration of MIR microcombs, single mode operation and anomalous dispersion of the waveguides, close to zero dispersion, are preferable,^{27,28} ideally in a small cross section waveguide to boost nonlinear effects. Cross section waveguide dimensions of $w = 3.25\ \mu\text{m}$ and $h = 3.3\ \mu\text{m}$ lead to the group velocity dispersion profile (D as a function of wavelength) for the TE₀ mode plotted in Fig. 1(c), with a broad anomalous regime between 3.5 and $4.8\ \mu\text{m}$ wavelength and single mode operation.

The ring radius was targeted to be as small as possible to reduce both the device footprint and, eventually, the threshold powers for nonlinear processes, while still being large enough not to be significantly impacted by bending losses. An $R = 250\ \mu\text{m}$ value was obtained, corresponding to a free spectral range (FSR) of $53\ \text{GHz}$. Bending losses are expected to be below $0.05\ \text{dB/cm}$ from mode solver simulations. A straight bus waveguide was designed to side couple light to the ring resonator [see Fig. 1(a)] with a coupling gap of $240\ \text{nm}$, the smallest gap achievable by deep-UV lithography. We probed our resonators using free-space butt-coupling to the bus waveguide, and due to our sufficiently large mode diameter, mode adaptors on the end-facets were not necessary. A summary of all design parameters is provided in Fig. 1(a).

The ring resonators were fabricated on a $200\ \text{mm}$ CMOS pilot line at CEA-Leti. The $3.3\ \mu\text{m}$ thick $\text{Si}_{0.6}\text{Ge}_{0.4}$ layer was grown by epitaxy on a Si substrate. The choice of a 40% Ge concentration resulted in an alloy with a wide transparency window, high nonlinearity, and low propagation loss because of a limited number of misfit dislocations. Deep ultraviolet lithography was then used to pattern the waveguides followed by deep reactive ion etching. More details on the fabrication can be found in the supplementary material of Ref. 16. In addition, the etching process was optimized for fabricating the small $0.24\ \mu\text{m}$ gap. This was needed to meet the difficulties in fabricating large aspect ratio structures,²⁹ in this case $3.3\ \mu\text{m}/0.24\ \mu\text{m} \approx 14$. Beside the rings, some serpentine waveguides (waveguides with a large number of subsequent bends) were also fabricated to determine bending losses [Fig. 1(f)]. Scanning electron microscope (SEM) pictures of a fabricated ring are shown in Figs. 1(d) and 1(e). As shown in Fig. 1(e), the gap was reliably obtained.

III. LOSS AND RESONANCE MEASUREMENT

Before characterizing the ring resonator, the bending loss was measured to estimate the achievable intrinsic quality factor and to validate the choice of bending radius. To characterize the losses, we used a tunable optical parametric amplifier (OPA) pulsed laser source (MIROPA-fs, Hotlight Systems) with $5\ \text{mW}$ input power, set at $3.9\ \mu\text{m}$. The power was chosen low enough to stay in the linear loss regime and not be influenced by the three and four photon absorption present in SiGe at this wavelength.¹⁷ The bending loss

was determined by measuring the transmission in TE polarization through waveguides with a large number of subsequent bends (serpentine waveguides) and different bending radii (68 – 212 bends depending on the radius, adding around $1\ \text{cm}$ of length) and comparing this to a $2.2\ \text{cm}$ long straight reference waveguide. The total loss (propagation + bending loss) measured on the serpentine waveguides for increasing bend radii is shown in Fig. 2 for a waveguide width of $3.25\ \mu\text{m}$. We repeated this study for slightly larger waveguide widths (3.50 and $3.75\ \mu\text{m}$) but did not observe any clear effect on the bending loss, showing that the mode was well confined for these waveguide widths. For $R = 250\ \mu\text{m}$, the loss is around $0.2\ \text{dB/cm}$. In fact, for this radius, the loss contribution caused by the bends becomes negligible as the propagation losses for serpentine waveguides with $R = 250\ \mu\text{m}$ and the straight waveguide ($R = \infty$) are indistinguishable within the measurement accuracy, which is consistent with our simulated bending loss estimation. These measurements are also in line with our previous demonstration of low propagation loss in the range of 0.1 – $0.4\ \text{dB/cm}$ in straight SiGe waveguides for similar waveguide dimensions and wavelengths.³⁰ The loss α and the intrinsic Q-factor Q_{in} are related through $Q_{in} = (10/\ln 10) \cdot (2\pi n/\alpha\lambda)$. Using this, the measured loss of $0.2\ \text{dB/cm}$ indicates that an intrinsic Q-factor $Q_{in} = 1\,170\,000$ should be achievable for the ring resonator.

Next, we characterized the ring resonators and measured their Q-factor. Figure 3(a) shows the measurement setup. The ring resonance characterization was performed using a narrow-linewidth continuous wave Adtech distributed feedback quantum cascade laser (QCL) with a small tuning range around $4.18\ \mu\text{m}$. The out-coupled light was recorded using either a PbSe photodetector or a Thorlabs Fourier transform infrared (FTIR) optical spectrum analyzer. The emission wavelength of the QCL was wavelength modulated between 4177.27 and $4177.89\ \text{nm}$ by applying a periodic triangular current modulation, which, as a side effect, also resulted in a power modulation of roughly $\pm 50\%$. The time-average optical pump power was set at around $20\ \text{mW}$ (measured directly before the input coupling lens), which is well below the onset of nonlinear losses as $4.18\ \mu\text{m}$ is beyond the three photon absorption cutoff and four photon absorption is negligible.¹⁷

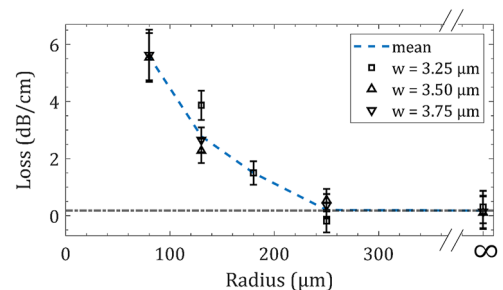


FIG. 2. Loss measurement in TE polarization for SiGe waveguides as a function of bending radius at $3.9\ \mu\text{m}$ wavelength. The total loss includes the bending loss and propagation loss. For radii larger than $250\ \mu\text{m}$, there is no additional bending loss: indicated by the black dashed line, the loss in the bends then becomes equal to the propagation loss measured for a straight waveguide, i.e., with $R = \infty$. The measurement is shown for different waveguide widths. As no clear trend for dependence on the width was observed in this case, the blue dashed line shows the mean across the three widths.

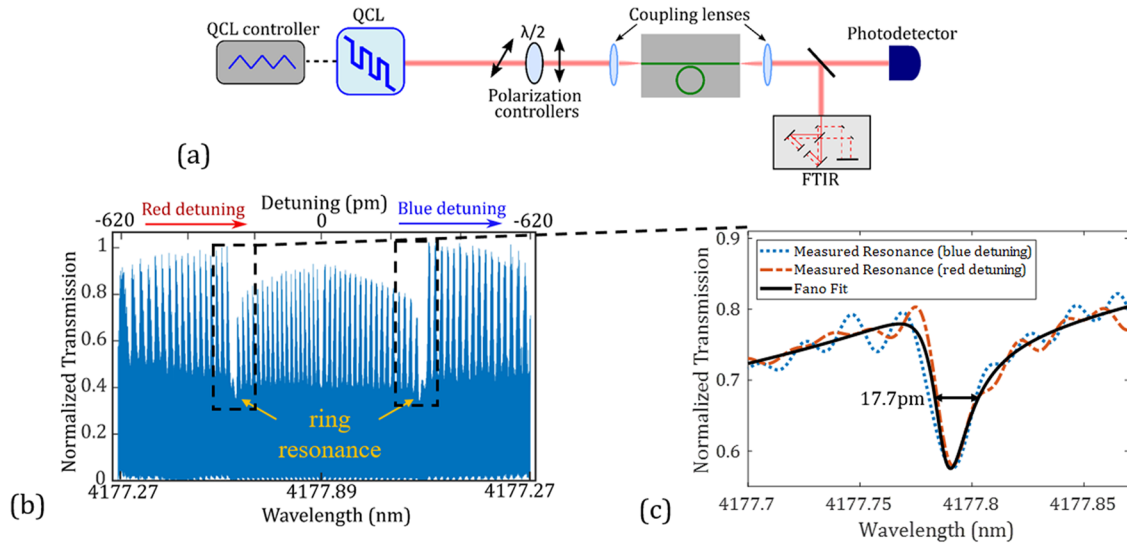


FIG. 3. (a) Experimental setup for Q-factor measurement. The light source is a quantum cascade laser (QCL) tunable around a wavelength of $4.18 \mu\text{m}$. A controller is used to apply a current modulation to modulate the wavelength. Polarizers and waveplates are used for polarization and input power control. MIR coupling lenses are used to butt couple the light in and out the waveguide. The output is recorded using either a photodetector or an FTIR. (b) Measurement of the ring resonance by FTIR. Wavelength scan with the QCL through the resonance (ramp up and ramp down). The ring resonance at one specific wavelength can be clearly distinguished from the Fabry–Perot resonances, which occur due to waveguide facets at input and output coupling. (c) Zoom-in on the ring resonance. A Fourier-filtering is applied to remove Fabry–Perot resonances. Due to the Fano shape of the resonance, a Fano function is fitted to it, resulting in a width of 17.7 pm corresponding to $Q = 236\,000$.

Figure 3(b) shows one period of the triangular wavelength modulation recorded by the FTIR. The triangular power modulation was subtracted (raw data shown in the supplementary material, Fig. 1). Over the whole wavelength range, there are pronounced Fabry–Perot resonances with a FSR of around 17 pm . These are caused by reflections at the chip end-facets that are 2.2 cm apart. Superimposed on these fringes, the ring resonance can be clearly distinguished: it manifests as an additional dip occurring twice, during the wavelength ramp up and ramp down, respectively. Figure 3(c) shows the ring resonance after applying Fourier filtering to filter out the Fabry–Perot fringes. Some low-amplitude oscillations are visible as remainders of the Fabry–Perot resonances. No significant difference is observed between blue and red detuning, indicating that there are no thermal effects.

It can be seen that the resonance exhibits a Fano line shape that was fitted with the Fano line shape function,³¹

$$\sigma(E) = \Delta^2 \frac{(q + \Omega)^2}{1 + \Omega^2}, \quad (1)$$

where $E = hc/\lambda$ is the energy, $\sigma(E)$ is the spectrum, $q = \cot(\delta)$ is the Fano parameter, δ is the phase shift between the coupled states, $\Delta = 4 \sin^2(\delta)$, and $\Omega = 2(E - E_0)/\Gamma$, in which Γ is the resonance width and E_0 is the resonance energy. Taking E_0 , Γ , and δ as free parameters, the measurement of Fig. 3(c) was well fitted with this equation (red line) using the following values: $\Gamma = 18.7 \text{ pm}$, $\delta = 0.37\pi$, $q = 0.64$, and $\Delta = 1.7$. The value for Γ corresponds to a loaded Q-factor of $236\,000 \pm 25\,000$, where the uncertainty was estimated through averaging over ten measurements of the same

resonance. The physical origin of this Fano shape requires further investigation. The q value indicates a mixed state between a Fano shape ($q = 1$) and a quasi-Lorentz shape ($q = 0$).

It can also be seen from Fig. 3(b) measurements that the resonance does not reach the noise floor and, instead, we have a transmission around 50% at resonance. This means that we are not at critical coupling ($Q_{in} = Q_{ext}$, where Q_{ext} is the external or coupling quality factor) and that the intrinsic quality factor of the ring (Q_{in}) is actually larger than the measured loaded Q-factor ($1/Q_{loaded} = 1/Q_{in} + 1/Q_{ext}$). A detailed discussion on the coupling regime can be found in Sec. II of the supplementary material.

This result represents a Q-factor improvement by more than one order of magnitude among Ge-based integrated microcavities, as can be seen from Table I. Our rings could, thus, be readily used for a range of sensing applications. This result is still a factor 3.4 smaller than the current record in the MIR range across all integrated platforms, held by SOI with a loaded Q around $800\,000^8$ (derived value from data provided in reference). However, the measured loss is almost identical so the difference in Q-factor is likely because we are further away from critical coupling. Moreover, our demonstration was obtained at slightly longer wavelengths ($4.18 \mu\text{m}$ against $3.8 \mu\text{m}$ in Ref. 8). Most importantly, our Ge-based microresonators should also work deeper into the MIR range, as the SiGe core waveguide is transparent up to $15 \mu\text{m}$ while record-holding SOI cavities have increasing losses for wavelengths beyond $3.5 \mu\text{m}$. Our operation at $4.18 \mu\text{m}$ wavelength was, indeed, only limited here by the wavelength of our laser, and these results should, thus, be easily extendable to longer wavelengths. According to our propagation loss measurements on this platform,³⁰ we know that reducing the losses

by another factor of 2 should be possible for the exact same material platform by optimizing the ring design (for example by choosing a lower loss wider waveguide and compensating for the decrease in coupling by Pulley or racetrack coupling schemes). This was also confirmed with our bending loss measurements, with possibly intrinsic Q-factors of 10^6 in a future fabrication run.

IV. CONCLUSION

To conclude, we have reported a SiGe ring resonator operating around $4.18\ \mu\text{m}$, with a loaded Q-factor of 236 000. This is the highest Q-factor achieved on this material platform and among the highest achieved around this wavelength range on a CMOS-compatible platform in general. Considering the demonstrated potential of the SiGe material platform, these rings should exhibit similarly high Q-factors at longer wavelengths, deeper in the MIR range. Measured losses in bent waveguides as low as 0.2 dB/cm for $250\ \mu\text{m}$ bend radius show that even higher Q-factors should be achievable on this material platform. These results set the basis for various sensing applications in the MIR spectral range. We also target further improvements of the Q-factor to be able to achieve threshold powers low enough for experimentally demonstrating nonlinear processes. This would be another milestone at these wavelengths.

SUPPLEMENTARY MATERIAL

See the supplementary material for the raw FTIR scan and the discussion on the coupling regime.

ACKNOWLEDGMENTS

We acknowledge the support of the Horizon 2020 research and innovation program under the Marie Skłodowska-Curie Actions (Grant No. ECLAUSion, 801512), the Agence Nationale de la Recherche (ANR) (Grant Nos. MIRSICOMB, ANR-17-CE24-0028; MIRthFUL, ANR-21-CE24-0005), and the International Associated Laboratory in Photonics between France and Australia (LIA ALPhFA). This work benefitted from a France 2030 government grant managed by the French National Research Agency (Grant No. ANR-22-PEEL-0005).

AUTHOR DECLARATIONS

Conflict of Interest

The authors have no conflicts to disclose.

Author Contributions

R.A. and M.P. contributed equally to this work.

Rémi Armand: Conceptualization (lead); Data curation (equal); Formal analysis (equal); Investigation (equal); Writing – review & editing (equal). **Marko Perestjuk:** Data curation (equal); Formal analysis (equal); Investigation (equal); Writing – original draft (lead); Writing – review & editing (lead). **Alberto Della Torre:** Data curation (supporting); Formal analysis (supporting);

Investigation (supporting); Visualization (equal); Writing – review & editing (equal). **Milan Sinobad:** Conceptualization (equal); Visualization (supporting); Writing – review & editing (supporting). **Arnan Mitchell:** Conceptualization (supporting); Funding acquisition (equal); Supervision (equal); Validation (supporting); Writing – review & editing (supporting). **Andreas Boes:** Supervision (equal); Validation (equal); Writing – review & editing (equal). **Jean-Michel Hartmann:** Methodology (equal); Writing – review & editing (equal). **Jean-Marc Fedeli:** Methodology (equal). **Vincent Reboud:** Methodology (equal); Writing – review & editing (supporting). **Pierre Brianceau:** Methodology (equal). **Alfredo De Rossi:** Formal analysis (equal); Software (equal); Validation (supporting). **Sylvain Combré:** Software (supporting); Validation (supporting); Writing – review & editing (equal). **Christelle Monat:** Conceptualization (equal); Funding acquisition (equal); Supervision (equal); Validation (equal); Writing – review & editing (equal). **Christian Grillet:** Conceptualization (equal); Funding acquisition (lead); Supervision (equal); Validation (equal); Writing – review & editing (equal).

DATA AVAILABILITY

The data that support the findings of this study are available from the corresponding author upon reasonable request.

REFERENCES

- R. Soref, “Mid-infrared photonics in silicon and germanium,” *Nat. Photonics* **4**, 495–497 (2010).
- D. Thomson, A. Zilkie, J. E. Bowers, T. Komljenovic, G. T. Reed, L. Vivien, D. Marris-Morini, E. Cassan, L. Viot, J.-M. Fédéli, J.-M. Hartmann, J. H. Schmid, D.-X. Xu, F. Boeuf, P. O’Brien, G. Z. Mashanovich, and M. Nedeljkovic, “Roadmap on silicon photonics,” *J. Opt.* **18**, 073003 (2016).
- A. G. Griffith, R. K. W. Lau, J. Cardenas, Y. Okawachi, A. Mohanty, R. Fain, Y. H. D. Lee, M. Yu, C. T. Phare, C. B. Poitras, A. L. Gaeta, and M. Lipson, “Silicon-chip mid-infrared frequency comb generation,” *Nat. Commun.* **6**, 6299 (2015).
- M. Yu, Y. Okawachi, A. G. Griffith, N. Picqué, M. Lipson, and A. L. Gaeta, “Silicon-chip-based mid-infrared dual-comb spectroscopy,” *Nat. Commun.* **9**, 1869 (2018).
- P. Ma, D.-Y. Choi, Y. Yu, Z. Yang, K. Vu, T. Nguyen, A. Mitchell, B. Luther-Davies, and S. Madden, “High Q factor chalcogenide ring resonators for cavity-enhanced MIR spectroscopic sensing,” *Opt. Express* **23**, 19969–19979 (2015).
- Y. Sun and X. Fan, “Optical ring resonators for biochemical and chemical sensing,” *Anal. Bioanal. Chem.* **399**, 205–211 (2011).
- C. J. Smith, R. Shankar, M. Laderer, M. B. Frish, M. Loncar, and M. G. Allen, “Sensing nitrous oxide with QCL-coupled silicon-on-sapphire ring resonators,” *Opt. Express* **23**, 5491–5499 (2015).
- S. A. Miller, M. Yu, X. Ji, A. G. Griffith, J. Cardenas, A. L. Gaeta, and M. Lipson, “Low-loss silicon platform for broadband mid-infrared photonics,” *Optica* **4**, 707 (2017).
- K. Luke, Y. Okawachi, M. R. E. Lamont, A. L. Gaeta, and M. Lipson, “Broadband mid-infrared frequency comb generation in a Si_3N_4 microresonator,” *Opt. Lett.* **40**, 4823–4826 (2015).
- R. Shankar, I. Bulu, and M. Loncar, “Integrated high-quality factor silicon-on-sapphire ring resonators for the mid-infrared,” *Appl. Phys. Lett.* **102**, 051108 (2013).
- Y. Zou, S. Chakravarty, C.-J. Chung, X. Xu, and R. T. Chen, “Mid-infrared silicon photonic waveguides and devices [Invited],” *Photonics Res.* **6**, 254 (2018).
- J. Haas, P. Artmann, and B. Mizaikoff, “Mid-infrared GaAs/AlGaAs micro-ring resonators characterized via thermal tuning,” *RSC Adv.* **9**, 8594–8599 (2019).

- ¹³L. Zhang, A. M. Agarwal, L. C. Kimerling, and J. Michel, "Nonlinear group IV photonics based on silicon and germanium: From near-infrared to mid-infrared," *Nanophotonics* **3**, 247–268 (2014).
- ¹⁴J. M. Ramirez, Q. Liu, V. Vakarini, J. Frigerio, A. Ballabio, X. Le Roux, D. Bouville, L. Vivien, G. Isella, and D. Marris-Morini, "Graded SiGe waveguides with broadband low-loss propagation in the mid infrared," *Opt. Express* **26**, 870 (2018).
- ¹⁵L. Carletti, P. Ma, Y. Yu, B. Luther-Davies, D. Hudson, C. Monat, R. Orobtcouk, S. Madden, D. J. Moss, M. Brun, S. Ortiz, P. Labeye, S. Nicoletti, and C. Grillet, "Nonlinear optical response of low loss silicon germanium waveguides in the mid-infrared," *Opt. Express* **23**, 8261–8271 (2015).
- ¹⁶M. Sinobad, C. Monat, B. Luther-davies, P. Ma, S. Madden, D. J. Moss, A. Mitchell, D. Allieux, R. Orobtcouk, S. Boutami, J.-M. Hartmann, J.-M. Fedeli, and C. Grillet, "Mid-infrared octave spanning supercontinuum generation to 85 μm in silicon-germanium waveguides," *Optica* **5**, 360 (2018).
- ¹⁷M. Sinobad, A. DellaTorre, R. Armand, B. Luther-Davies, P. Ma, S. Madden, A. Mitchell, D. J. Moss, J.-M. Hartmann, J.-M. Fedeli, C. Monat, and C. Grillet, "Mid-infrared supercontinuum generation in silicon-germanium all-normal dispersion waveguides," *Opt. Lett.* **45**, 5008–5011 (2020).
- ¹⁸M. Montesinos-Ballester, C. Lafforgue, J. Frigerio, A. Ballabio, V. Vakarini, Q. Liu, J. M. Ramirez, X. Le Roux, D. Bouville, A. Barzaghi, C. Alonso-Ramos, L. Vivien, G. Isella, and D. Marris-Morini, "On-chip mid-infrared supercontinuum generation from 3 to 13 μm wavelength," *ACS Photonics* **7**, 3423–3429 (2020).
- ¹⁹A. Della Torre, M. Sinobad, R. Armand, B. Luther-Davies, P. Ma, S. Madden, A. Mitchell, D. J. Moss, J.-M. Hartmann, V. Reboud, J.-M. Fedeli, C. Monat, and C. Grillet, "Mid-infrared supercontinuum generation in a low-loss germanium-on-silicon waveguide," *APL Photonics* **6**, 016102 (2021).
- ²⁰B. Troia, J. S. Penades, A. Z. Khokhar, M. Nedeljkovic, C. Alonso-Ramos, V. M. N. Passaro, and G. Z. Mashanovich, "Germanium-on-silicon vernier-effect photonic microcavities for the mid-infrared," *Opt. Lett.* **41**, 610–613 (2016).
- ²¹J. M. Ramirez, Q. Liu, V. Vakarini, X. Le Roux, J. Frigerio, A. Ballabio, C. Alonso-Ramos, E. T. Simola, L. Vivien, G. Isella, and D. Marris-Morini, "Broadband integrated racetrack ring resonators for long-wave infrared photonics," *Opt. Lett.* **44**, 407–410 (2019).
- ²²D. A. Kozak, N. F. Tyndall, M. W. Pruessner, W. S. Rabinovich, and T. H. Stievater, "Germanium-on-silicon waveguides for long-wave integrated photonics: Ring resonance and thermo-optics," *Opt. Express* **29**, 15443–15451 (2021).
- ²³S. Radosavljevic, N. T. Beneitez, A. Katumba, M. Muneeb, M. Vanslembrouck, B. Kuyken, and G. Roelkens, "Mid-infrared Vernier racetrack resonator tunable filter implemented on a germanium on SOI waveguide platform [Invited]," *Opt. Mater. Express* **8**, 824 (2018).
- ²⁴D. Ren, C. Dong, S. J. Addamane, and D. Burghoff, "High-quality microresonators in the longwave infrared based on native germanium," *Nat. Commun.* **13**, 5727 (2022).
- ²⁵F. Ottonello-Briano, C. Errando-Herranz, H. Rödjegård, H. Martin, H. Sohlström, and K. B. Gylfason, "Carbon dioxide absorption spectroscopy with a mid-infrared silicon photonic waveguide," *Opt. Lett.* **45**, 109 (2019).
- ²⁶See <https://www.lumerical.com> for Ansys lumerical.
- ²⁷C. Godey, I. V. Balakireva, A. Coillet, and Y. K. Chembo, "Stability analysis of the spatiotemporal L-Lefever model for Kerr optical frequency combs in the anomalous and normal dispersion regimes," *Phys. Rev. A* **89**, 063814 (2014).
- ²⁸J. S. Levy, A. Gondarenko, M. A. Foster, A. C. Turner-Foster, A. L. Gaeta, and M. Lipson, "CMOS-compatible multiple-wavelength oscillator for on-chip optical interconnects," *Nat. Photonics* **4**, 37–40 (2009).
- ²⁹I. W. Rangelow, "Critical tasks in high aspect ratio silicon dry etching for microelectromechanical systems," *J. Vac. Sci. Technol., A* **21**, 1550–1562 (2003).
- ³⁰A. D. Torre, R. Armand, M. Sinobad, K. F. Fiaboe, B. Luther-Davies, S. Madden, A. Mitchell, T. Nguyen, D. J. Moss, J.-M. Hartmann, V. Reboud, J.-M. Fedeli, C. Monat, and C. Grillet, "Mid-infrared supercontinuum generation in a varying dispersion waveguide for multi-species gas spectroscopy," *IEEE J. Sel. Top. Quantum Electron.* **29**, 1–10 (2022).
- ³¹M. F. Limonov, M. V. Rybin, A. N. Poddubny, and Y. S. Kivshar, "Fano resonances in photonics," *Nat. Photonics* **11**, 543–554 (2017).